J. Fluid Mech. (2025), *vol.* 1007, A84, doi:10.1017/jfm.2025.51

JFM PAPERS

Ribbing patterns in inertial rotary drag-out

J. John Soundar Jerome[1], **Pierre Trontin**[1] **and Jean-Philippe Matas**[1]

[1]Universite Claude Bernard Lyon 1, LMFA, UMR5509, CNRS, Ecole Centrale de Lyon, INSA Lyon, Villeurbanne 69622, France

Corresponding author: J. John Soundar Jerome, john-soundar@univ-lyon1.fr

(Received 12 June 2024; revised 21 December 2024; accepted 22 December 2024)

We report pattern formation in an otherwise non-uniform and unsteady flow arising in high-speed liquid entrainment conditions on the outer wall of a wide rotating drum. We show that the coating flow in this rotary dragout undergoes axial modulations to form an array of roughly vertical thin liquid sheets which slowly drift from the middle of the drum towards its sidewalls. Thus, the number of sheets fluctuates in time such that the most probable rib spacing varies ever so slightly with the speed, and a little less weakly with the viscosity. We propose that these axial patterns are generated due to a primary instability driven by an adverse pressure gradient in the meniscus region of the rotary drag-out flow, similar to the directional Saffman–Taylor instability, as is wellknown for ribbing in film-splitting flows. Rib spacing based on this mechanistic model turns out to be proportional to the capillary length, wherein the scaling factor can be determined based on existing models for film entrainment at both low and large capillary numbers. In addition, we performed direct numerical simulations, which reproduce the experimental phenomenology and the associated wavelength. We further include two numerical cases wherein either the liquid density or the liquid surface tension is quadrupled while keeping all other parameters identical with experiments. The rib spacings of these cases are in agreement with the predictions of our model.

Key words: pattern formation

1. Introduction

A gas/liquid interface is rarely uniform. It is often irregular with defects such as bubbles and drops. It is nevertheless common that two-phase flows, even in the most complex situations, exhibit robust patterns such as waves, rivulets, cells, ridges and finger-like structures. In many cases, the primary characteristics of such pattern formation can be elucidated through the analysis of the flow stability and/or via phenomenological models

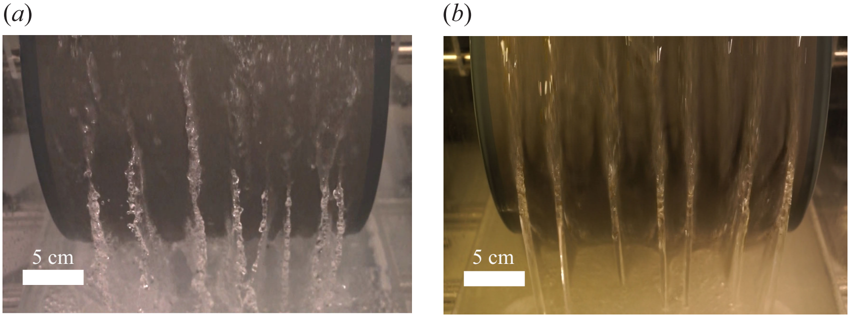

Figure 1. Examples of ribbing patterns, i.e. sheets of liquid, rising vertically out of the reservoir in relatively regular spacing along the axis of a rotating drum in (*a*) water, linear velocity 3.8 m s^{-1} and (*b*) water/ UCON mixture of approximately 100 times the viscosity of water, 1.6 m s^{-1}. Both photos correspond to the case when the working liquid covers 10 % of the drum radius at rest.

(Cross & Hohenberg 1993; Fauve 1998; Gallaire & Brun 2017). An example of ordered pattern formation in an otherwise non-uniform and seemingly random free-surface flow is reported here, for the case of liquid film entrainment along a rotating wheel. This is also relevant to understanding the liquid load that be can left over a moving substrate during dragout, as for example, by car wheels on a wet road, journal bearings at high-operational speeds and rapid roll coating processes which exhibit misting i.e. atomisation of the entrained liquid film flow.

We consider a circular drum of radius R which is only partly immersed in a liquid of viscosity μ, density ρ and surface tension σ. Let $\varOmega$ be its angular speed. Analogous to the celebrated two-dimensional (2-D) plate drag-out problem treated by Landau & Levich (1942) and Deryaguin (1943), the rotating drum entrains a liquid film over its outer surface if its linear speed $U = R\varOmega$ is more than the dewetting speed. Recently, we pointed out that as the drum is rotated at faster rates one or more liquid sheets appear on the emerging side depending on the drum width (John Soundar Jerome *et al.* 2021, see figures 4 and 5, and references therein). Here, in figure 1, we display instantaneous images of an array of liquid sheets that occur for a much wider drum in our present experiments, and for two liquids which differ in their dynamic viscosity by a factor 100. As the drum speed is increased steadily, the quasi-static meniscus along the axis of the cylinder deforms into a regular pattern of thin liquid sheets with a thick rim (see figure 2). The sheet height increases as the square of the drum speed, similar to the case of a single sheet in front of a horizontal rotating disc in a liquid bath (John Soundar Jerome *et al.* 2021). The goal of the present work is to elucidate the mechanism at the origin of these liquid sheets.

Yih (1960) was the first to consider the theoretical prediction of ribbing patterns in the context of Fourdrinier machines (A device that features a rotating drum in a tank of pulp and water for producing a continuous web of paper by draining the mixture on a specially meshed conveyor belt.) in the paper industry. He performed a linear stability analysis of a base flow which consists of a thin, freelyrotating film in the absence of gravity and viscous shear at the liquid/gas interface. Thereby, he observed that the critical wavelength λ_Y is only weakly, or negligibly, dependent on the film Reynolds number $Re_f = (UR/\nu)(\delta_f/R)^2$, where $\nu = \mu/\rho$ is the kinematic viscosity and δ_f is the film thickness which was manually metered in his experiments. From both theory and experiments, Yih (1960) further demonstrated that λ_Y is strongly dependent on wheel radius, angular speed and the liquid surface tension σ via the Weber number $We = \rho U^2 R/\sigma$ so that $\lambda_Y \simeq 2\pi R\sqrt{3/We}$. This is primarily due to the fact that the driving mechanism for the instability is the centripetal

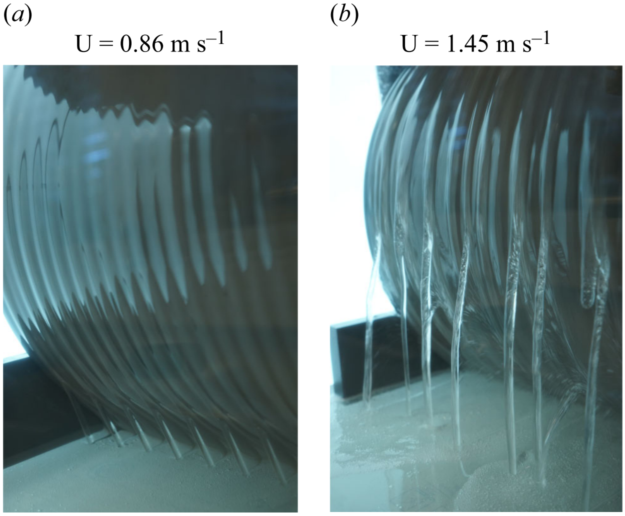

Figure 2. Images of ribbing patterns at two different speeds in the viscous UCON/water mixture (photo credits: R. Cates) for the same wheel immersion conditions as above.

acceleration. So, Yih's ribbing instability is analogous to Taylor vortices (Taylor 1923) occurring in a liquid bound between two rotating cylinders, wherein the outer cylinder wall is replaced by a free-surface boundary condition. A similar axial instability is also known in the case of external rimming flows (Moffatt 1977, see figures 5–9). While analysing the existence of steady solutions for the case of a slowlyrotating thin viscous film on the outer surface of a circular cylinder, Moffatt (1977) observed ring-like patterns along the axis of the cylinder in his experiments. Surprisingly, these patterns occurred even at speeds as small as 12 rpm. He suggested that such patterns in a viscous rotating film are not only due to centrifugal forces but also driven by gravity and shear forces, which are neglected in Yih's (1960) analysis. To the authors' present knowledge, the role of centrifugal forces in such a simple wall-driven viscous film flow is still an open question. Many investigations of ribbing and cellular patterns can be found in the case of internal rimming flows (Balmer 1970; Thoroddsen & Mahadevan 1997) wherein a fixed quantity of liquid inside a cylinder is subject to rotation, see figure 3(*a*). Hosoi & Mahadevan (1999) analysed the rimming flow case for small volume fraction of liquid i.e. up to 6 % of the cylinder volume. By including inertia, along with gravity, capillarity and viscous forces, they attributed the onset of the axial instability to the presence of a localised liquid ridge of reverse flow in the thin film, as depicted in figure 3(*a*). Such a ridge appears when the rescaled Reynolds number $Re = \epsilon U R/\nu$ is of $\mathcal{O}(1)$ where $\epsilon = \delta_g/R$ is a small parameter, if $\delta_g = \sqrt{\nu U/g}$ is the relevant length scale for the film thickness due to a balance between acceleration due to gravity (g) and viscous shear arising from the moving wall. Thus, any perturbation in the axial direction leads to thick film regions draining much faster into the ridge than thinner ones, since gravitational effects are stronger in the former while the wall shear stress is more important in the latter region. Thereby, the ridge height continues to vary along the cylinder axis until surface tension forces become significant due to the free-surface curvature along the cylinder axis. In addition, the authors proposed that the wavelength of the most unstable mode is proportional to $L_R Ca^{-1/3}$, where $Ca = \mu U/\sigma$ is the capillary number and L_R is some typical ridge height.

Ribbing was also often observed in film-splitting flows (Schweizer & Kistler 2012) that occur when the outer wall of one or more rollers drag a liquid film from a reservoir, in

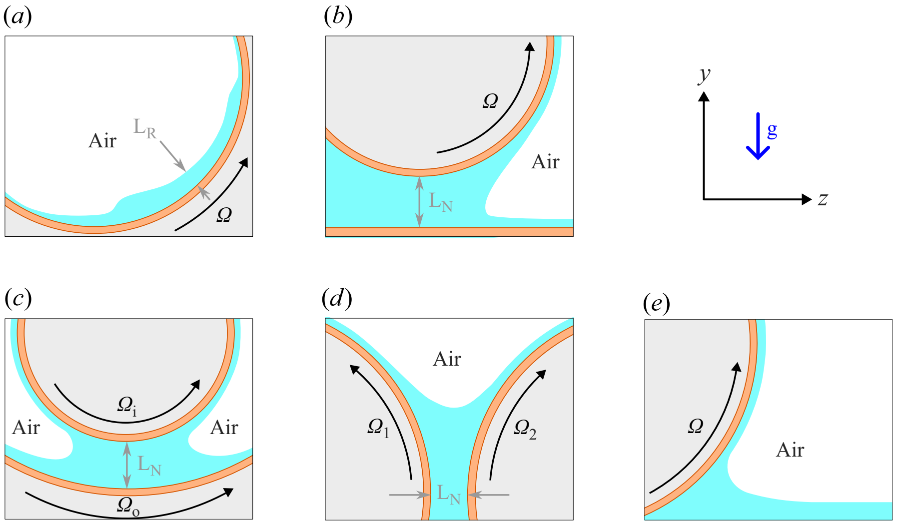

Figure 3. Schematic view (not to scale) of previous investigations on axial pattern formation in coating flows on the outside and the inside of a cylinder for (*a*) rimming flows with liquid ridge as elucidated by Hosoi & Mahadevan (1999) and (*b*)–(*d*) film-splitting flows resulting in a thin film on one or more a rotating substrate, as studied by Adachi *et al.* (1988), Rabaud (1994) and Coyle *et al.* (1990), respectively. (*e*) The present configuration is analogous to the film-splitting case but the meniscus region is free to evolve away from the cylinder. Also, the Reynolds number based on the film thickness is approximately 10^2–10^4 in our study.

the presence of a strong confinement. A few such thin viscous coating flow configurations are illustrated in figure 3(*b*–*d*), where the minimum gap is usually much smaller than the roller radius i.e. $L_N \ll R$. In this context, a largebody of investigation is available for what is now commonly referred to as the 'printer's instability', wherein a regular axial variation of film thickness occurs in the widening gap between two rotating cylinders, see figure 3(*c*) (Pitts & Greiller 1961; Mill & South 1967; Savage 1977; Coyle *et al.* 1990; Hakim *et al.* 1990; Rabaud 1994). Ribbing in this configuration is often discerned when the capillary number is sufficiently large, depending on the confinement ratio L_N/R. For a given liquid viscosity and surface tension, the number of ribs (n_r) increases rapidly with the roller speed and then it saturates at larger velocities. Also, a smaller number of ribs are observed as rollers are kept further apart i.e. L_N/R is increased. The gap L_N is typically of the order of 10 µm to 1 mm, and the distance between ribs varies between a few hundreds of micrometres to a few millimetres. Gravity can be disregarded in the nip and a Couette–Poiseuille flow is imposed in the neighbourhood of the meniscus, resulting from a balance between the wall-imposed shear stress and mass conservation. An adverse pressure gradient is therefore present close to the interface, and leads to the formation of fingers which progressively stretch away from the meniscus. Ribbing in this configuration is analogous to the directional Saffman–Taylor instability (Saffman & Taylor 1958; Hakim *et al.* 1990; Rabaud 1994; Reinelt 1995). In general, the rib spacing λ decreases as $Ca^{-1/2}$ when the capillary number is increased; however, at sufficiently large capillary numbers, it saturates to a constant value depending on the gap as $\lambda \propto L_N^{2/3}$, where the constant of proportionality is a function of the liquid physical properties , and the nip geometry (Adachi *et al.* 1988, see figures 6 and 7), since the latter precisely fixes both the meniscus location and the adverse pressure gradient experienced by the static air/liquid interface. Finally, these regular ribbing patterns become unstable and result in spatio-temporal chaos as the capillary number is further increased (Couder *et al.* 1990; Michalland *et al.* 1996).

A related pattern formation occurs in liquid film flows over the end of a flat or a curved plate. Depending on the mass flux imposed by the source, Pritchard (1986) illustrated that the overflowing liquid film flow could break into dripping droplets and liquid columns along the streamwise direction. At larger flow rates, a rich dynamical behaviour is observed (Giorgiutti *et al.* 1995; Limat *et al.* 1997, see references therein). The underlying mechanism is due to the Rayleigh–Taylor instability when a thin liquid film is accelerated towards a less dense fluid. This is also at the origin of patterns known as rivulets on thin viscous films flowing under an inclined flat or a curved plate (Balestra *et al.* 2018; Ledda *et al.* 2020; Lerisson *et al.* 2020). In all these cases, the characteristic wavelength of the primary instability is proportional to the film thickness which is fixed by the source which feeds the film flow, or the initial coating film thickness. Furthermore, the wall is static whereby the film flow is driven only by gravity in the absence of an externally imposed wall shear.

The present article concerns ribbing patterns such as those shown in figure 1 that arise from a situation of coating flows depicted in figure 3(*e*). The aforementioned draining, rimming and film-splitting flows belong to a class of coating flows where the Reynolds lubrication approximation is valid i.e. the Reynolds number $Re_f = (UR/\nu)(\delta_f/R)^2$, which is based on the linear velocity U and the entrained liquid film thickness δ_f, is either small or $\mathcal{O}(1)$ at best. Inertia plays little role in these wall-driven liquid entrainment flows, except maybe for the ridge formation in internal rimming flows, as in figure 3(*a*). In our study, we are interested in flow regimes where inertia is no longer negligible since Re_f becomes as large as 10^4 in some cases. Figure 1(*a*) shows that the rims of the liquid sheets break-up and result in atomisation. Therefore, in many experiments in water and at high-speed cases in the viscous water/UCON mixture, droplets detach from ribs, and air bubbles which are entrained in the plunging film below the wheel are re-entrained within the ribs. Also, the ribs themselves experience strong fluctuations in shape and position.

Under these conditions, full-scale numerical simulations are difficult and costly. Therefore, a phenomenological approach is adopted here to investigate pattern formation in liquid drag-out flow at very large Reynolds numbers ($Re_f \gg 1$). We begin by presenting our experimental set-up and then by describing our observations and results in § 2. In § 3, we propose a mechanism based on the directional Saffman–Taylor instability in order to predict the characteristic distance between ribs. Finally, we present in § 4 the results of a numerical simulation of this problem, and discuss the consistency of the obtained results with our model.

2. Experimental observations

2.1. *Materials, set-up and methods*

The set-up is illustrated in figure 4. Here, a wheel of radius $R = 19.5$ cm and width 30 cm, partially immersed in a reservoir, is rotated about its horizontal axis, entrained by an asynchronous motor, coupled with a Parker AC10 AC inverter drive. The wheel is made out of a thick PVC tube and its axis is a rigid steel bar of 25 mm diameter which is one metre long. It is mounted on three ball bearings, with a pair of them on each side of the drum (approximately 40 cm) and the last one closer to the motor. We regularly verified that no visible precession about the cylinder axis occurred when the drum is under rotation. In the following, the distance between the wheel bottom and the free surface of the liquid at rest is denoted by H. The bottom of the wheel is located at 6.3 cm above the tank floor. For all our experiments, we use either water, or a mixture of water and UCON oil (300 g of UCON for 700 g of water). The composition of the latter is controlled before each series of experiments by properly measuring the mixture density with an Anton

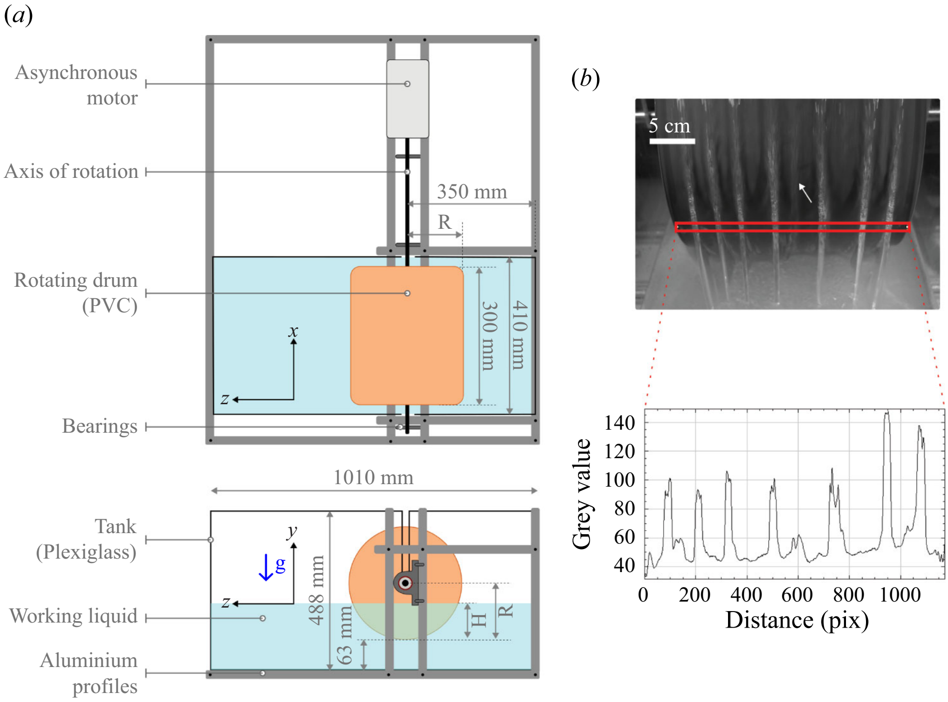

Figure 4. (*a*) Top and side view schematics of experimental set-up depicting the liquid tank and the partially immersed rotating drum. Water depth can be changed to control the drum immersion, such that $H/R \in [0, 1]$. (*b*) Snapshot displaying the front view of a typical ribbing pattern and the corresponding intensity profile for the case of water/UCON mixture when $H/R = 0.1$ and $U = 1.6\ \mathrm{m\ s^{-1}}$ (see supplemental movies I, II and III). The white arrow indicates an incipient rib between two other ribs which are drifting apart from each other.

Liquid	Density (ρ) $\mathrm{kg\ m^{-3}}$	Viscosity (μ) $\times 10^{-3}$ Pa s	Surface tension (σ) $\times 10^{-3}$ N m
Water	999 ± 1	1.05 ± 0.02	70 ± 2
70 % water-30 % UCON$^{\mathrm{TM}}$ 3($WU3$)	1045 ± 1	90 ± 9	58 ± 2

Table 1. Properties of liquids used in the present work. UCON$^{\mathrm{TM}}$ Lubricant 75-H-90,000 was used for all mixtures used here.

Paar DMA35 densimeter (precision $10^{-4}\ \mathrm{g\ cm^{-3}}$), and the temperature of the mixture. Note that the dynamic viscosity (μ) of the water/UCON mixture can be as high as 100 times that of water (see table 1). However, variations in temperature between different series of experiments with the water/UCON mixture can lead to changes in viscosity of the order of 15 %. Therefore, throughout this article, whenever the experimental results for a water/UCON mixture are presented, the reader shall be referred to its corresponding viscosity value. Special care was taken to wash the tank thoroughly every time we changed the liquid from the water/UCON mixture to just water. Traces of UCON in water readily led to vigorous foaming without any marked influence on the unsteady, non-uniform character of the observed ribbing. The effect of surfactant on the rib shape and sheet break-up is beyond the scope of present study.

Images of the liquid structures generated when the liquid is dragged out by the wheel are recorded with the help of a Sony $\alpha 7$ camera. A typical image of ribbing patterns

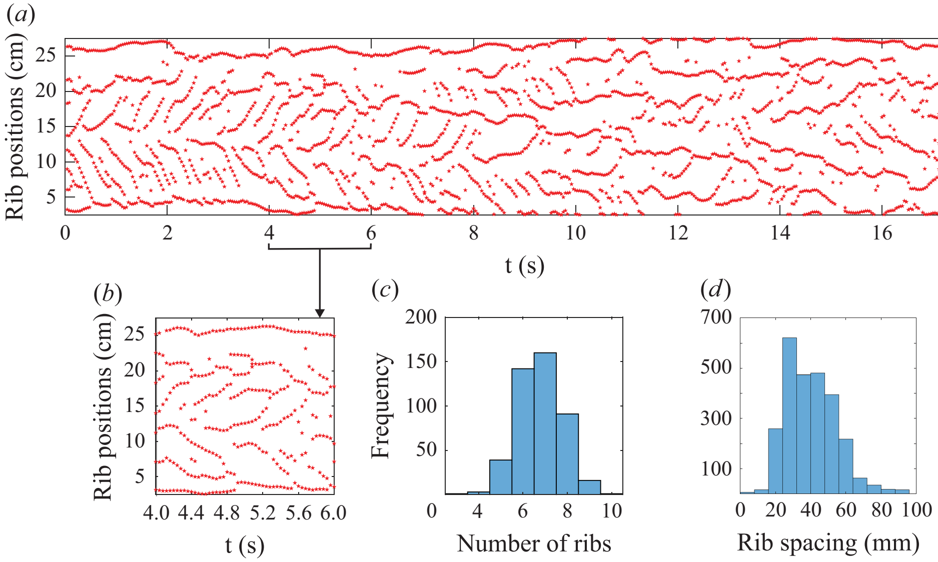

Figure 5. (*a*)–(*b*) Spatio-temporal evolution of rib positions, $H/R = 0.05$ and $\Omega = 73$ rpm, water/UCON mixture $\mu = 0.096$ Pa s, frame rate 25 images/s (see supplemental movie I). The range of positions on the vertical axis covers the total width of the wheel, 30 cm. (*c*)–(*d*) Histograms of number of ribs and rib spacing for the same conditions.

recorded by the camera is displayed in figure 4(*b*)-top. We can extract from such an image the associated intensity profiles along the width of the wheel (figure 4*b*-bottom). Both the image and its intensity profile are then analysed with Matlab to identify the location of each rib for each image. This procedure is carried out for at least 1000 images for experiments with water/UCON mixtures, and 1500 images for experiments with water. Each of these image counts correspond to a video duration of at least 40 and 60 seconds, respectively.

2.2. *Evolution of rib spacing over time*

Figure 5 shows a typical spatio-temporal diagram over 18 seconds for the water/UCON mixture (the frame rate is 25 images/s for all acquisitions). This diagram shows that the ribs formed near the edges of the wheel are mostly pinned to the same location, while the ribs located near the centre of the wheel tend to travel to the nearest edge. This process can also be observed in figure 4(*b*), where a small rib, indicated by a white arrow, is emerging midway between both sides, as the two ribs next to it migrate to opposite sides. The resulting distributions of the total number of ribs and of distances between neighbouring ribs are displayed in figures 5(*c*) and 5(*d*) respectively. The distribution of inter-rib distances is not symmetric. In particular, very large inter-rib distances can be observed due to outward drift of ribs as inferred from the spatio-temporal diagram.

In figure 1, the ribs observed with both water and the water/UCON mixture present spacings of the same order of magnitude, in spite of the very different values in viscosity for both liquids. However, the flow is strongly inertial for the case of water, for which, as mentioned in the introduction, the Reynolds number based on the rib thickness can be as high as 10^4. Indeed, the impact of viscosity is visible on the rim of liquid sheets and the sheet smoothness in both images displayed in figure 1. Thus, for the less viscous case (water), we observe that the sheet is strongly distorted, and droplets may even detach from the rib as water is ejected from the wheel (see supplemental movie I). The corresponding spatio-temporal diagram and histograms for the number of ribs and inter-rib distances are

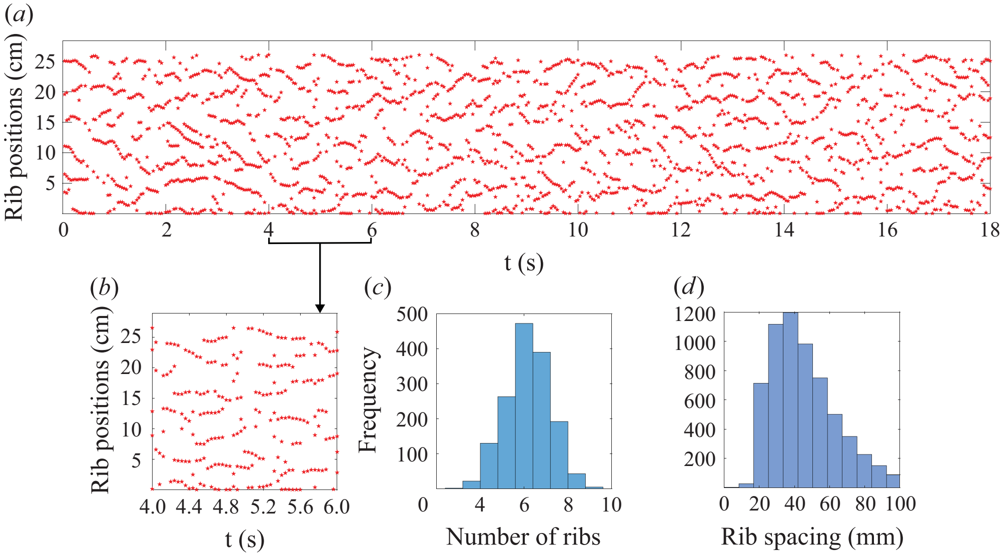

Figure 6. (*a*)–(*b*) Spatio-temporal evolution of rib positions, $H/R = 0.05$ and $\Omega = 122$ rpm, water, frame rate 25 images s^{-1} (see supplemental movie I). (*c*)–(*d*) Histograms of number of ribs and inter-rib distances for the same conditions.

shown in figure 6 for the case of water. The same features as for the viscous water/UCON case are again observed for the dynamics of the liquid sheets i.e. the ribs close to the edge remain approximately pinned to their location, while ribs formed midway between the edges tend to travel to the closer side. The strong fluctuations in rib shape, which introduce noise in rib detection, render the tracking of ribs a little more difficult than in figure 5(*a*). A satisfying convergence for typical histograms of rib spacing can nonetheless be obtained, if the recording duration is extended to 60 seconds for the water series.

For both water and water/UCON mixtures, the histograms of the number of ribs are approximately symmetric, and exhibit close to normal distributions. In contrast, the histograms of the inter-rib distances are asymmetric.

In what follows, we chose to retain the maximum value of the latter histogram as a relevant measure of the distance between ribs for a given set of conditions, rather than the mean value which would lead to overestimate the rib spacing. Note that this value is computed from a parabolic fit based on the histogram maximum and its two adjacent values. Hereafter, this value will be referred simply as rib spacing λ, for the sake of brevity. Experiments performed by decreasing the distance between the wheel and the tank bottom down to 1 cm did not show any impact on either the rib spacing or the above mentioned rib dynamics. Therefore, results given in the remainder of the paper were all obtained for a fixed distance of 6.3 cm between the wheel and the tank floor, as in figure 4(*a*).

2.3. *The most probable rib spacing*

We show in figure 7 the distribution of the measured inter-rib spacing along with the maximum (symbol ∘) of the rib spacing histogram as a function of wheel rotation velocity, and for four immersion depths H/R. The results of this figure are all for the 30 % UCON and 70 % water mixture. The small variations in viscosity between each series correspond to the variation in temperature between them.

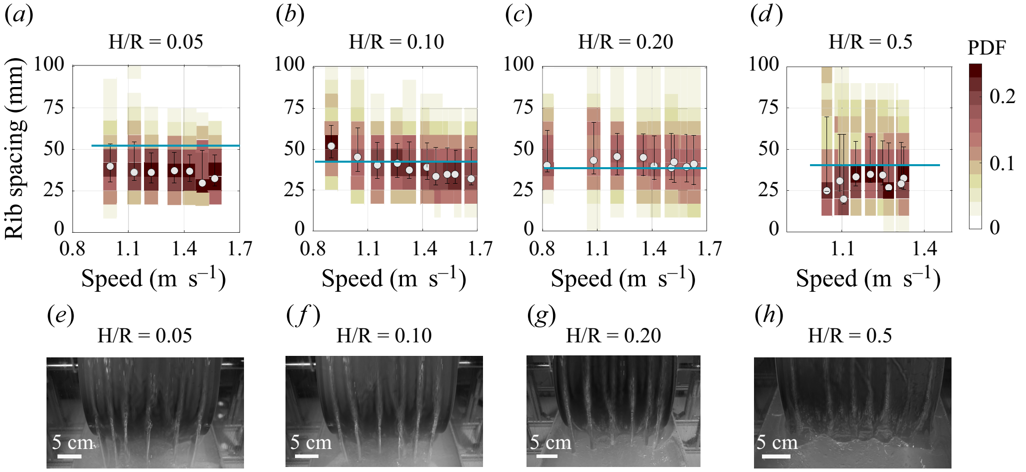

Figure 7. Variations of the most probable rib spacing (○) as a function of velocity U, for 30 % water/UCON mixture, and for different immersion depths H/R: (*a*) $H/R = 0.05$ and $\mu = 0.096$ Pa.s, (*b*) $H/R = 0.1$ and $\mu = 0.099$ Pa.s, (*c*) $H/R = 0.2$ and $\mu = 0.081$ Pa.s, (*d*) $H/R = 0.5$ and $\mu = 0.095$ Pa.s Error bars indicate the values of the first and last quartiles. Colour bar represents the normalised PDF values from the histogram of the inter-rib distances. All instant photographs in (*e*)–(*g*) correspond to the velocity $U = 1.4 \pm 0.1$ m s^{-1}, while it is 1.25 m s^{-1} for (*h*) $H/R = 0.5$. Continuous line (cyan) in each figure was computed using expression (3.14) based on *directional* Saffman–Taylor instability. See supplemental material for movies.

The measured rib spacing values are similar for all depths, of the order of 4 cm. The lower and upper error bars indicate the values of the first and last quartiles, respectively. The main observation is that the rotation speed has no significant impact on the rib spacing. At $H/R = 0.5$, Supplemental movies II and III show that the rib thickness becomes of the order of magnitude of the rib spacing, which limits rib formation at low velocities, as illustrated in figure 7(*h*). Note also that, as mentioned in the introduction, bubbles are generated when air is entrained on the plunging side of the wheel, or when the ribs fall back into the bath. They are present below the wheel and can be further entrained along with the working liquid. These bubbles tend to move into the ribs, and to regroup in lines as they are swept on the other side along the surface of the wheel. These bubbles are the reason why the upper part of the ribs appears in a lighter shade (see figure 7). The rib spacing values measured for $H/R = 0.5$ at velocities lower than 1.25 m s^{-1} correspond to the spacing between these bubble trails. Their values are of the same order of magnitude as for the rib spacing measured at lower H/R. Figure 8 presents the evolution of the most probable rib spacing as a function of velocity for experiments carried out with water. For the sake of completeness, the inter-rib spacing distribution is also provided for each case investigated here. The measured values are close to, but slightly smaller than, the values for the water/UCON mixture, with typical rib spacings of the order of 3.5 cm. The same slight decrease of rib spacing with velocity is observed for the three smaller immersion depths. This decrease is observed in the position of the most probable spacing (symbol ○), but also in the positions of the first and fourth quartiles, which are slightly shifted to lower values when the speed is increased. As observed for the water/UCON mixture, no significant influence of the immersion depth is observed on the rib spacing in figure 8(*e*–*h*), even though the thickness of the ribs varies dramatically between $H/R = 0.05$ and $H/R = 0.5$. Note that the effect of surface roughness, using for example a bubble wrap (not shown here), hardly changed these observations.

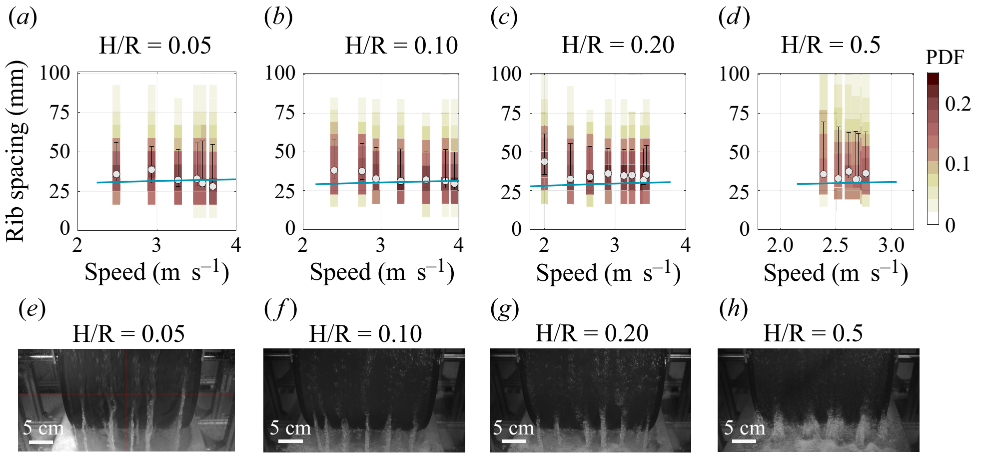

Figure 8. Variations of the most probable rib spacing (∘) as a function of velocity U, for water at different immersion depths H/R: (*a*) $H/R = 0.05$, (*b*) $H/R = 0.1$, (*c*) $H/R = 0.2$ and (*d*) $H/R = 0.5$. Colourbar represents the normalised PDF values from the histogram of the inter-rib distances. All illustration photographs (*e*)–(*h*) correspond to velocities close to 2.7 m s^{-1}. Continuous line (cyan) in each figure was computed using expression (3.14) based on directional Saffman–Taylor instability.

3. Mechanism of pattern formation

As discussed in the introduction, the observed ribbing patterns are very similar to those already observed for the Rayleigh–Taylor (RT) instability of a thin liquid films falling under gravity, or under centrifugal acceleration. They also resemble those observed in directional Saffman–Taylor (ST) instability of wall-entrained viscous liquid in thin diverging gaps. The maximum growth rate of infinitesimal perturbations in the RT case is well known (Vrij 1966; Babchin *et al.* 1983; Fermigier *et al.* 1992; Mikaelian 1996; Balestra *et al.* 2018)

$$\omega_i^{RT} \sim \frac{\rho^2 g_a^2 \delta_f^3}{\mu\sigma}, \tag{3.1}$$

where δ_f is the film thickness and g_a is the apparent acceleration equal to the effective acceleration due to gravity, or U^2/R. In the ST case, its expression from Hakim *et al.* (1990) and Rabaud (1994) can be simplified as follows:

$$\omega_i^{ST} \sim \left(\frac{U}{\delta_f}\right) Ca^{1/2}, \tag{3.2}$$

where the driving pressure gradient of the base flow has been taken as $\mu U/\delta_f^2$. For water, with $g = 9.81\ \mathrm{m\,s^{-2}}$ and $\delta_f \sim \sqrt{\mu U/\rho g} Ca^{1/6}$ (Landau & Levich 1942; Wilson 1982), we get $\omega_i^{ST} \sim 750\ \mathrm{s^{-1}}$ while $\omega_i^{RT} \sim 5\ \mathrm{s^{-1}}$. For the viscous UCON/water mixtures in our experiments $Ca > 1$ and so, we take $\delta_f \sim 2/3\sqrt{\mu U/\rho g}$ (Deryaguin 1943; Jin *et al.* 2005). Then, the orders of magnitude of the growth rates are 550 s^{-1} and 130 s^{-1}, respectively, in the case of linear ST and RT instability.

These values suggest that the directional ST mechanism is perhaps the most suited for the observed patterns in our experiments. Nonetheless, using $g_a = U^2/R$ when $U = 2\ \mathrm{m\,s^{-1}}$ quadruples the RT growth rate. Also, the RT growth rate is not very small when compared with that of the ST case for the UCON/water mixtures even at speeds of $U \approx 1\ \mathrm{m\,s^{-1}}$ and $g_a = 9.81\ \mathrm{m\,s^{-1}}$. So, the RT mechanism might not be negligible at

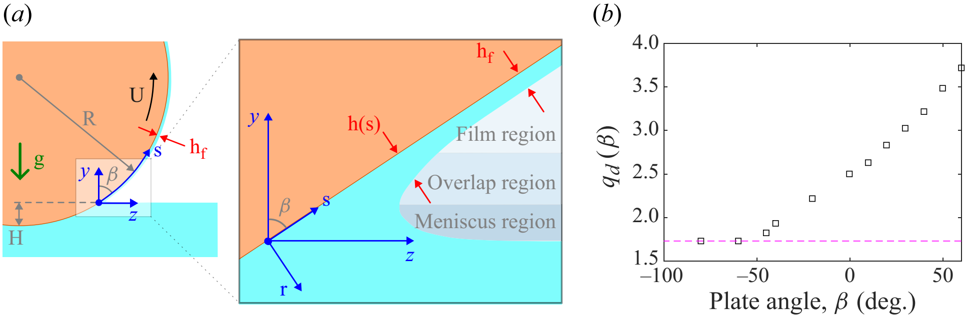

Figure 9. (*a*) Schematic of the rotary drag-out problem and its equivalent inclined flat-plate LLD flow where $\beta = \sin^{-1}(1 - H/R)$ with s the curvilinear coordinate such that $s = 0$ at the point of intersection between the liquid level at rest and the wheel. Note that $h(s)$ in the overlap region generally decreases as $s > 0$ increases down to the asymptotic value h_f in the fullydeveloped film region. (*b*) The second prefactor $q_d(\beta)$ in the expression (3.9) is estimated from the maximum flow rate condition via the Stokes equation at $Ca >> 1$ (Jin *et al.* 2005, figure 8).

highspeeds, for the viscous case in our study. However, the rib spacing did not evolve considerably when we doubled (UCON/water), or even quadrupled (water), the drum speed. Furthermore, advection is strong in our experiments, contrary to the case of a falling liquid film.

Thus, following previous investigations on ribbing patterns in thin film-splitting coating flows and rimming flows (Pitts & Greiller 1961; Mill & South 1967; Adachi *et al.* 1988; Coyle *et al.* 1990; Hakim *et al.* 1990; Rabaud 1994), we expect that the driving mechanism in our study is due to an adverse pressure gradient on the rising side of the rotating drum. We now proceed to demonstrate the existence of this adverse pressure gradient in the rotary drag-out flow, and then relate its magnitude to the characteristic wavelength of a linear directional ST instability. For the sake of simplicity, the analysis is restricted to the2-D inclined-plate drag-out problem.

3.1. *Pressure gradient in the drag-out problem*

Consider the2-D rotary drag-out problem is illustrated in figure 9(*a*), wherein an infinitelylong horizontal rotating cylinder entrains a liquid out of a bath. Similar to the classical LandauLevich–Deryaguin (LLD) (Landau & Levich 1942; Deryaguin 1943) flat-plate dragout, the flow field can be distinguished into a fullydeveloped film region and a meniscus region separated by an overlap region. Also, when the local film thickness $h(s) \ll R$, the velocity component, say u, along the curvilinear coordinate s is dominated by viscous shear. Therefore, in the film and the overlap region, 2-D lubrication theory should hold as long as the flow is quasi-parallel and the local Reynolds number based on the film thickness $Re_f = (\rho g R/\mu)(h_f/R)^2$ is small. Furthermore, as suggested by Wilson (1982), if the dynamic meniscus length is much smaller than the cylinder radius, it is possible to reduce the rotary dragout to an equivalent inclined flat-plate entrainment flow such that the plate angle with respect to the vertical is given by $\sin\beta = 1 - H/R$, where H is the immersion depth as depicted in figure 9(*a*). Under the lubrication approximation

$$0 = -\rho g \cos\beta - \frac{\partial p}{\partial s} + \mu \frac{\partial^2 u}{\partial r^2} + \mathcal{O}\left(Re_f\right), \tag{3.3}$$

$$0 = \rho g \sin\beta - \frac{\partial p}{\partial r} + \mathcal{O}\left(Re_f\right), \tag{3.4}$$

where p is the liquid pressure in the film. The boundary conditions are $u = U$ at the wall ($r = 0$), and $\partial u/\partial r = 0$ at $r = h(s)$. In the absence of any axial pressure gradient, the inclined LLD flow at firstorder is

$$u(r, s) = \frac{1}{2\mu}\left(\frac{\partial p}{\partial s} + \rho\tilde{g}\right)\left(r^2 - 2hr\right) + U, \tag{3.5}$$

where $\tilde{g} = g\cos\beta$ is the effective gravity. Now, by applying mass conservation i.e.

$$\frac{\mathrm{d}}{\mathrm{ds}}\left(\int_{r=0}^{r=h(s)} u(r, s)\mathrm{d}r\right) = 0, \tag{3.6}$$

between the overlap region and the film region (where $h(s) = h_f$ and $p(s, r) = P_0$, the atmospheric pressure) we get

$$\begin{aligned} -\frac{h^3}{3\mu}\left(\frac{\partial p}{\partial s} + \rho\tilde{g}\right) + Uh &= -\frac{h_f^3}{3\mu}\rho\tilde{g} + Uh_f, \\ \Rightarrow \frac{\partial p}{\partial s} &= -\rho\tilde{g}\left(1 - \frac{h_f^3}{h^3}\right) + \frac{3\mu U}{h^2}\left(1 - \frac{h_f}{h}\right), \end{aligned} \tag{3.7}$$

which can be rewritten after some algebra, and by defining the pressure gradient $G = \partial p/\partial s$, as follows:

$$G = -\rho\tilde{g}\left(1 - \frac{h_f}{h}\right)\left(1 + \frac{h_f}{h} - \left(a^2 - 1\right)\frac{h_f^2}{h^2}\right), \tag{3.8}$$

where parameter $a = \sqrt{3}Ca^{1/2}l_c/h_f$ with $l_c = \sqrt{\sigma/\rho\tilde{g}}$ the characteristic capillary length scale. It is customary to further relate the pressure gradient to the local film curvature via the YoungLaplace theorem and then obtain an expression for the film thickness $h(s)$. Thereupon, it is possible to obtain both the flow and pressure field (Weinstein & Ruschak 2001). It is also possible to include inertial effects (Cerro & Scriven 1980; Kheshgi *et al.* 1992; Weinstein & Ruschak 2004). In our formulation, however, all the details of the flow field are resumed in parameter a, which contains the filmthickness h_f. We estimate this parameter from the classical formulae for h_f under lubrication approximations. At small capillary numbers ($Ca \ll 1$), the film thickness is given by

$$h_f = \frac{0.9458\, l_c Ca^{2/3}}{\sqrt{\sec\beta + \tan\beta}}\left(1 - \frac{0.113}{\sec\beta + \tan\beta}Ca^{1/3} + \mathcal{O}(Ca^{2/3})\right), \tag{3.9}$$

which is the generalisation of Landau–Levich vertical drag-out flow (Landau & Levich 1942) to the case of an inclined flat plate for different $0 \leq \beta < \pi/2$ by Wilson (1982). At $Ca \gg 1$, $h_f \propto l_c Ca^{1/2}$, where the constant of proportionality depends on the plate inclination angle (β), as established by Jin *et al.* (2005), see figure 8. (This was first hypothesised by Deryaguin & Levi (1964) for the case of a vertical drag-out flow.) using direct numerical simulations of the Stokes equation for the inclined-plate drag-out problem. Therefore, we obtain

$$a = \begin{cases} q_w(\beta)\, Ca^{-1/6} + \mathcal{O}\left(Ca^{1/6}\right) & \forall Ca \ll 1, \\ q_d(\beta) & \forall Ca \gtrsim 1, \end{cases} \tag{3.10}$$

such that $q_w(\beta) = 1.06\sqrt{3(\sec\beta + \tan\beta)}$ and $q_d(\beta) \geq \sqrt{3}$, as presented in figure 9(*b*).

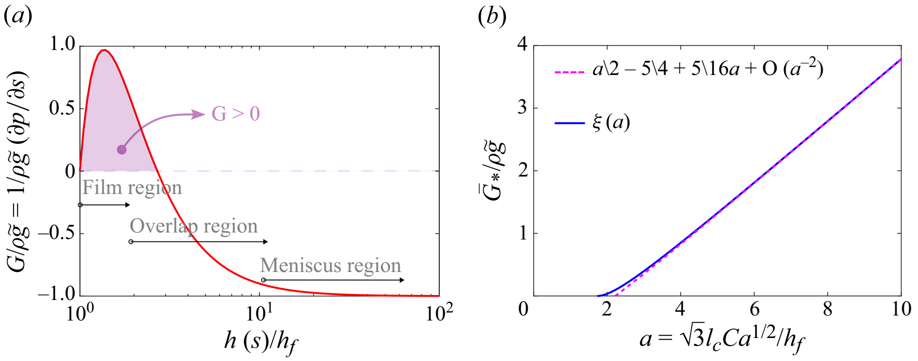

Figure 10. (*a*) Non-dimensional pressure gradient along the inclined flat plate as a function of the relative local film thickness $h(s)/h_f$ as computed from (3.8) with $a = 4$. (*b*) The average non-dimensional adverse gradient pressure is presented against the parameter $a > \sqrt{3}$ and shows that the series expansion of a in (3.13) compares well with the computed value from (3.12).

In figure 10(*a*), we present a typical evolution of the pressure gradient as a function of the normalised film thickness for $a = 4$. Firstly, in the meniscus region the relative film thickness $\tilde{h}(s) = h(s)/h_f \ll 1$, the pressure gradient here tends to its hydrostatic limit $G = -\rho\tilde{g}$. As the curvilinear coordinate $s > 0$ increases, in the overlap zone, the pressure gradient increases as well, since $h(s)$ decreases monotonically. Figure 10(*a*) shows that G reaches a maximum before decreasing to zero in the film region, where the film thickness $h(s) = h_f$. This implies that there exists a region of positive pressure gradient for the condition $a = 4$. More generally, in the overlap region adjacent to the film region shown in figure 9(*a*), we can admit that $h(s) \sim h_f(1+\epsilon)$, for some $\epsilon \ll 1$. Then, we find that

$$G \sim \rho\tilde{g}(a^2 - 3)\epsilon + \mathcal{O}(\epsilon^2). \tag{3.11}$$

This pressure gradient is of $\mathcal{O}(\epsilon)$ and positive if $a > \sqrt{3}$ (or in other words, $h_f < l_c Ca^{1/2}$). Thus, a necessary condition for an adverse pressure gradient to exist in the overlap zone is that the filmthickness is larger than the Jeffreys drainage lengthscale $l_c Ca^{1/2} \equiv \sqrt{\mu U/\rho\tilde{g}}$ (Jeffreys 1930). Furthermore, expression (3.8) indicates that $G(s) > 0$ as long as $h_f < h(s) < h_*$, where $h_* = (\sqrt{4a^2 - 3} - 1)h_f/2$ is the filmthickness at some location upstream of the film region ($h(s) \gtrsim h_f$). Thus, the pressure gradient G is positive for all $h_f < h(s) < h_*$. Thereby, we propose to estimate the average adverse pressure gradient in this zone as follows:

$$\bar{G}_* = \frac{1}{(h_* - h_f)} \int_{h_f}^{h_*} G(h)\mathrm{d}h \equiv \rho\tilde{g}\xi(a), \tag{3.12}$$

where $\xi(a)$ is some irrational function that increases monotonically with the parameter $a > \sqrt{3}$, as presented in figure 10(*b*). The general expression of $\xi(a)$ can be developed as a Laurent series

$$\xi(a) = \frac{a}{2} - \frac{5}{4} + \frac{5}{16a} + \mathcal{O}\left(\frac{1}{a^2}\right) > 0, \tag{3.13}$$

at sufficiently large values of a which, as depicted in figure 10(*b*), is a good approximation for $\xi(a)$ when $a \gtrsim 3$.

In summary, an adverse pressure gradient such as the one evidenced in figure 10(*a*) will exist in the neighbourhood close to the film region ($h(s) \gtrsim h_f$) provided $a > \sqrt{3}$. Its average scales as the absolute value of the hydrostatic pressure gradient $\rho\tilde{g}$ and some function of plate angle β and the capillary number Ca. The existence of an adverse pressure gradient could also be qualitatively inferred from the shape of the meniscus between the reservoir and the film region in a drag-out flow. However, the previous analysis does not rely upon any estimate of the meniscus curvature. Here, the pressure gradient arises directly out of a dynamic equilibrium in the presence of viscous shear, gravity and capillarity. The effect of capillarity is contained in the chosen model for film thickness h_f.

3.2. *Directional Saffman–Taylor instability in rotary drag-out flows*

The existence of a region of positive pressure gradient between the film and the overlap regions in the lubrication limit leads to the so-called directional ST instability (Hakim *et al.* 1990). Note that the ST instability in a porous medium, or a Hele-Shaw cell, refers to the situation when a fluid of viscosity μ_1 is displaced by another less viscous fluid when $\mu_2 < \mu_1$ (Saffman & Taylor 1958). Whereas, in the classical ST instability, the interface between the two immiscible fluids is under displacement towards the more viscous fluid, the meniscus in the LLD drag-out flow is immobile in the laboratory frame. However, in the frame of reference of the moving plate, the air/liquid interface can be seen as an advancing meniscus towards the more viscous fluid i.e. water or water/UCON mixtures in LLD flow. Furthermore, the pressure gradient is favourable as one moves across the interface from the less viscous fluid to the more viscous fluid. This is also the case for the drag-out problem in the reference frame attached to the moving plate. It is precisely in this sense that we propose the directional ST mechanism in the overlap region for the development of ribbing in inertial rotary drag-out flows.

For the case of a liquid of viscosity μ displaced by air, the most unstable wavelength λ_{ST} of the ST instability is given by $\lambda_{ST} \simeq \pi b\sqrt{\sigma/\mu V}$, where the viscosity of air has been neglected in comparison with that of the liquid, b is the thin gap between two horizontal plates and V is the speed at which the air/liquid interface advances (Saffman & Taylor 1958; Chuoke *et al.* 1959; Homsy 1987). This expression can be rewritten in terms of the driving pressure gradient, say G, as $\lambda_{ST} \simeq 2\pi\sqrt{3\sigma/|G|}$, since $G = -\mu V/12b^2$. In our case for the LLD flow, we expect that the wavelength λ_* of the most unstable axial perturbation is given by the average pressure gradient $\bar{G}_*$ in the neighbourhood of the film region where the pressure gradient is positive. So, we obtain

$$\lambda_* = 2\pi l_c\sqrt{3/\xi(a)}, \tag{3.14}$$

where $\xi(a)$ is the normalised average adverse pressure gradient in the overlap zone of the rotary drag-out problem as defined in (3.12), and $l_c = \sqrt{\sigma/\rho\tilde{g}}$ is the characteristic capillary length scale. By using the series expansion of $\xi(a)$ i.e, (3.13) along with the lubrication approximation (3.10) for the parameter $a = \sqrt{3}l_c Ca^{1/2}/h_f$ in the above relation, we estimate that $\lambda_* \sim 2\pi l_c\sqrt{3/q_w(\beta)}Ca^{1/12}$ at low capillary numbers $Ca \ll 1$ and $\lambda_* \sim 2\pi l_c\sqrt{3/q_d(\beta)}$ at $Ca \gg 1$, up to $\mathcal{O}(a^{-2})$. This implies that the mostunstable wavelength is expected to vary only very weakly with the capillary number $Ca = \mu U/\sigma$, and hence with velocity. This is consistent with the experimental observations that velocity has almost no impact on the rib spacing. This also means that the liquid density ρ and surface tension σ via the capillary length l_c must play an important role in the rib spacing.

Finally, we point out that the above expression (3.14) does not account for the spatial variation of the pressure gradient along the flow direction i.e. the curvilinear coordinate s. Also, in such a case where the pressure gradient is non-uniform, *linear* instability characteristics should be a function of the flow geometry. In fact, this has been done for the case of the Printer's instability (Coyle *et al.* 1990; Hakim *et al.* 1990; Rabaud 1994;

Reinelt 1995). Therefore, in order to build a more rigorous estimate of the wavelength for the case of the rotary LLD flow, a global stability analysis (Chomaz 2005; Theofilis 2011) is necessary. Even though this deserves further investigations, it is beyond the scope of the present work. Furthermore, the analysis should be adapted to incorporate liquid inertia since Re_f is rarely small in our experiments where ribbing is observed. Nevertheless, in the following, we propose to study the relevance of the estimation provided in (3.14) for the mostunstable wavelength by comparing it with experiments and simulations.

Continuous lines (cyan) in figures 7 and 8 are obtained using the above formula where the average adverse pressure gradient $\bar{G}_*$ is computed via (3.10) and (3.12) based on the lubrication approximation (Landau & Levich 1942; Deryaguin 1943; Wilson 1982; Jin *et al.* 2005). In our experiments, the capillary number is such that $0.03 < Ca < 0.06$ for water and $1.4 < Ca < 2.8$ for the water/UCON mixture. Within these ranges, the non-dimensional parameter $a = \sqrt{3} l_c Ca^{1/2}/h_f$ in expression (3.10) varies only between 2 and 4. For all data points in water/UCON mixtures (figure 7) and also, in water (figure 8), the proposed wavelength λ_* provides a good order of magnitude despite the variations in drum immersion H/R and drum speed U. This is all the more interesting from the fact that a basic ST analogy which includes only the average pressure gradient G_* from calculations based on an idealised 2-D lubrication model is quite relevant to predict the mostprobable rib spacing λ in our experiments wherein the flow is strongly inertial, unsteady, spatially non-uniform and three-dimensional.

4. Numerical experiments

The validity of the proposed scaling for the mostprobable rib spacing λ can be further elucidated via direct numerical simulations (DNS) of the rotating wheel configuration. To do so, the transient three-dimensional two-phase interfacial, incompressible Navier–Stokes equations are solved with the open-source software Basilisk (Popinet 2009, 2024). A spatially adaptive octree grid, particularly well suited to the multi-scale nature of the problem, is used. The maximum level of mesh refinement, noted here as N, refers to an equivalent Cartesian grid resolution having 2^N grid points in each direction. Here, N varies between 9 and 10, which is equivalentto 512^3 to 1024^3 points on a fixed grid. The interface between the two immiscible fluids is tracked with a sharp geometric volume-of-fluid (VOF) method. Basilisk is well designed for DNS of open inertial two-phase flows with large interface deformations (Zhang *et al.* 2020; Mostert *et al.* 2022) where realistic density and viscosity ratios, such as between water and air, can be considered. The computational domain is depicted in figure 11 (left). It consists of a cubic box of size $L_b = 80\,\mathrm{cm}$ and a half cylinder of radius $R = 20\,\mathrm{cm}$ and length $L_b = 80\,\mathrm{cm}$. The default symmetry boundary conditions are applied on all faces of the domain except the top face where a free outflow boundary condition is imposed. Wheel rotation is accounted for in the calculation by a penalty method in which a solid-body rotation of angular velocity $\Omega = U/R = 65$ rpm is forced on the half-cylinder. Note that the system is left to evolve freely without any initial perturbation but under the influence of numerical noise which is of the order of the smallest spatial step size. Initial perturbations of the wetting line as a controlled disturbance were tested as well (not shown here) for wavelengths, up to the order of L_b (the box size). The wavelengths obtained for the sheets were identical to those obtained without initial disturbance of the wetting line. See supplemental movie IV for the time evolution of interface from simulation data. The movie shows that the ribs appear quickly as the liquid starts to rise along the wheel: then, as the film slows down and thickens, a ‘top-down’ back flow starts to develop, which eventually plunges into the pool at the location of the ribs. Note that we were unable to realise simulations for

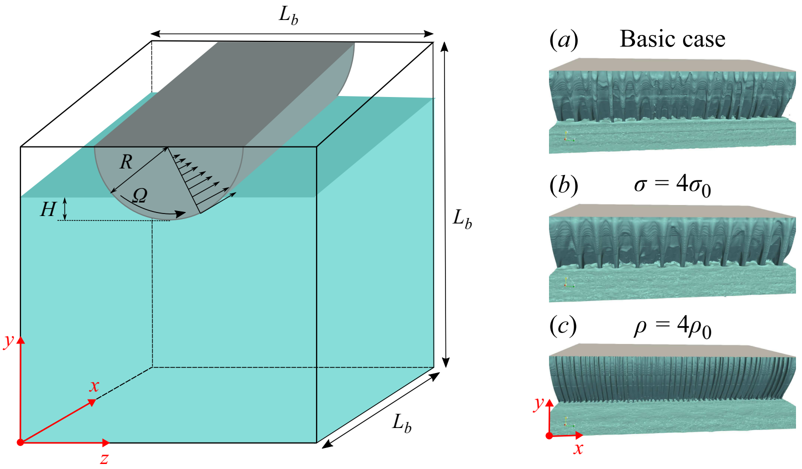

Figure 11. Computational domain and instantaneous ribbing patterns for three case studies using open-source DNS, namely, Basilisk. The box size is $L_b = 80$ cm and the cylinder radius is 20 cm. See supplemental movie IV for time evolution of the VOF for the three cases.

longer than 1 s in the best of the cases due to increase in computation time resulting from many drops and bubbles in the box. At the end of the simulation (see supplemental movie IV), once the ribs had developed, we discern a back flow along the ribs. Coarse-grained full cylinder simulations (not shown here) confirmed that this is not related to the liquid outflow boundary condition on the half-cylinder. As already shown for the case of a single rib for the case of a horizontal rotating disc (John Soundar Jerome *et al.* 2021), this should in turn influence the entrained flow over the cylinder downstream of the ribs. Note that the finite size of the cylinder length in our experimental set-up promotes rib undulations and meandering. This is further accentuated by the presence of droplets and bubbles in experiments. These effects are less important in our simulations, where a symmetrical boundary condition is imposed at cylinder ends. We recall that DNS was used to compute characteristics rib spacing and growth rates for various liquid properties. The nonlinear effects due to end and top boundary conditions are not within the scope of the present numerical study.

A reference case, termed the basic case hereafter, was first run to compare the observed mostprobable inter-rib distance λ for the case of the water/UCON mixture at $U = 1.36\ \mathrm{m\,s^{-1}}$ and $H/R = 0.2$. Here, the liquid density, viscosity and surface tension are $\rho_0 = 1044\ \mathrm{kg\,m^{-3}}$, $\mu_0 = 100$ Pa s and $\sigma_0 = 0.05\ \mathrm{N\,m^{-1}}$, respectively. Note that these physical parameters correspond precisely to one of the experimental runs, see figure 7(*g*). Furthermore, two sets of numerical experiments were treated in order to test the proposed scaling with the capillary length l_c. For these cases, we modified either the liquid surface tension to $\sigma = 4\sigma_0$, or the liquid density to $\rho = 4\rho_0$, while keeping all other parameters identical to the basic case. The computed iso-surfaces for VOF $= 0.5$ are shown in figure 11(*a–c*). All cases present a large number of ribs along the cylinder axis while the ribbing patterns vary between the different cases studied here. Approximately 52 ribs are observed in the case where the liquid density is exactly 4 times the basic case i.e. $\rho = 4\rho_0$. This is just approximately twice the number of ribs in the basic case, and about four times that obtained in the case when only the liquid surface tension is modified to $\sigma = 4\sigma_0$ (see supplemental movie IV). These observations show a good qualitative agreement with the proposed scaling for the rib spacing, since the latter scales with the capillary length $l_c = \sqrt{\sigma/\rho\tilde{g}}$, as indicated by expression (3.14).

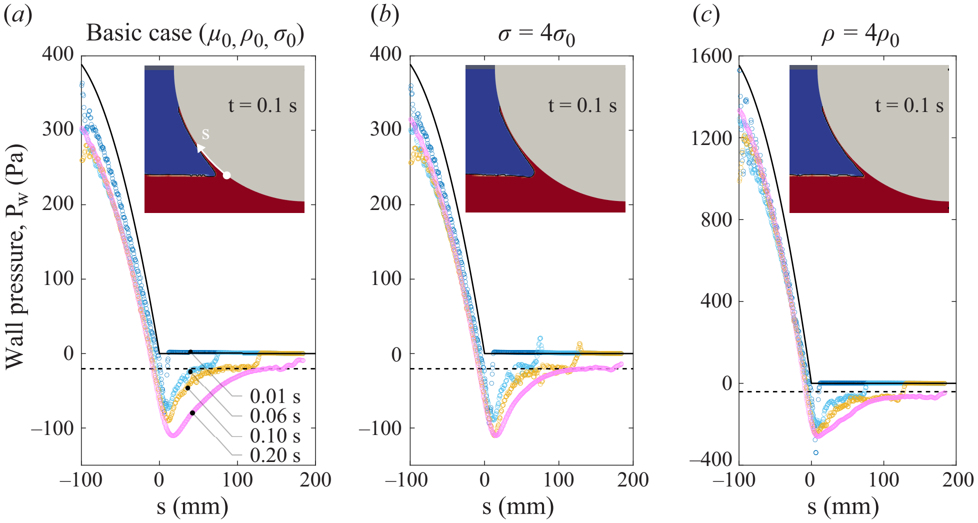

Figure 12. Pressure profiles along the curvilinear coordinate, s, within the entrained liquid film in the midplane ($x = 40$ cm), at four different timesteps: (*a*) basic case ; (*b*) $\sigma = 4\sigma_0$; (*c*) $\rho = 4\rho_0$. The continuous and dashed lines (black) correspond respectively to the hydrostatic case when the wheel is at rest and to the radial pressure gradient $\rho U^2/R$ in the film region.

We plot in figure 12 the instantaneous liquid pressure profile on the drum wall for each of the cases studied here using Basilisk at different timesteps, as the liquid film is entrained over it. Note that the x-axis is the curvilinear coordinate s, as defined previously in figure 9(*a*), and the contribution from the atmospheric pressure P_{atm} has been subtracted out, i.e. $P_w = 0$ in air. The thick continuous line (black) represents wall pressure if the wheel were at rest. Therefore, it simply corresponds to the hydrostatic pressure underneath the liquid surface (for all $s < 0$) and the atmospheric pressure when $s \geq 0$. As time increases, we observe that the pressure profiles very slightly deviate from the hydrostatic case, as long as $s \lesssim 0$. Thereafter, the wall pressure P_w dips below the line $P_w = 0$ to reach a minimum, before raising back towards the atmospheric pressure. This further confirms the presence of an adverse pressure gradient ($G > 0$) between the meniscus and the film. In this overlap region, it can be remarked that the pressure profiles continue to evolve in time for all cases studied here. Insets in figure 12 display the snapshots of the VOF (red liquid; blue – air; black – interface) at $t = 0.1$ s. As expected, the film thickness for the case when only density is quadrupled is much thinner than the other two cases since the thickness in the film region typically scales with the length $\delta_f \propto \sqrt{\mu U/\rho \tilde{g}}$, if the capillary number is $\mathcal{O}(1)$ (Jin *et al.* 2005). Moreover, in this zone, the centripetal acceleration on a fluid particle should be balanced out, at the leading order, by a radial pressure gradient i.e. $\partial p/\partial r = \rho u^2/R$. Therefore, the pressure close to the wall should fall below P_{atm} down to $\mathcal{O}(-\rho U^2 \delta_f/R)$, since the pressure at the free surface is equal to the atmospheric pressure due to the negligibly small contribution from interface curvature. This value is indicated by the horizontal dashed lines in figure 12, which shows a good match with the pressure data from computations in a small region whose extent varies with time, t. As we move away from this zone, P_w increases as we approach the front of the entrained liquid film and thereafter, $P_w = 0$ on the wall outside the film. Finally, it is pointed out here that the maximum adverse pressure gradient evolves in time and attains a value 30 % smaller than what is estimated by the lubrication model (3.13). This might arise from the fact that (i) in simulations, the pressure profiles are very sensitive to the spatial resolution of the

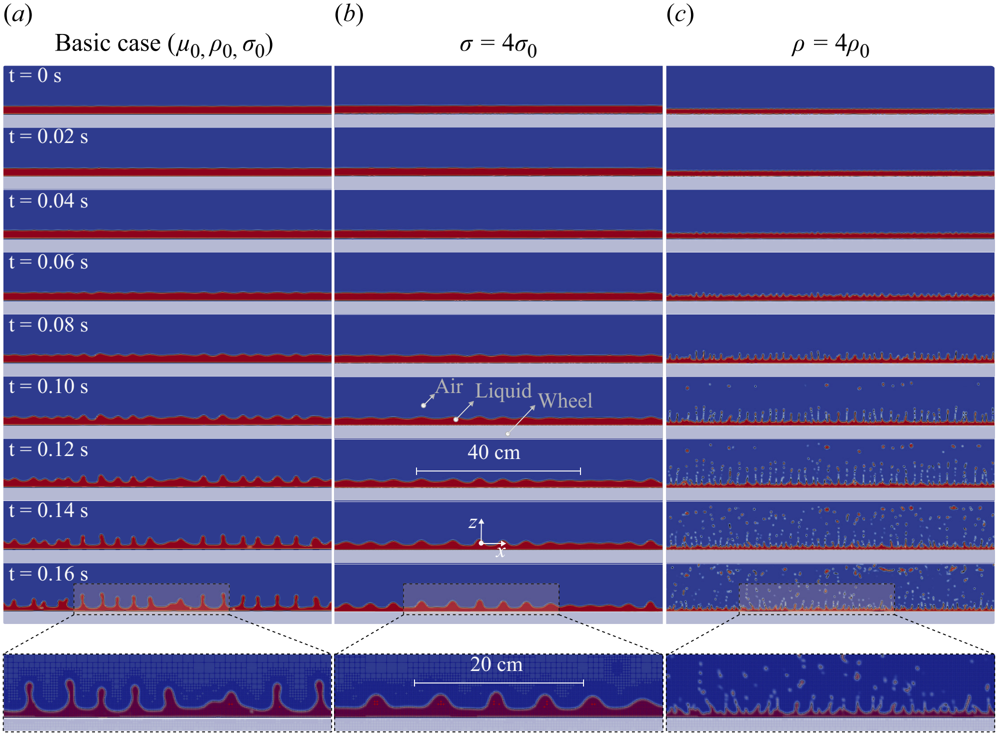

Figure 13. Temporal evolution of the ribbing patterns in our DNS using Basilisk (Popinet 2009, 2024). Here, the basic case corresponds to the water/UCON mixture ($\rho_0 = 1044\ \mathrm{kg\ m^{-3}}$, $\mu_0 = 100\ \mathrm{Pa\ s}$ and $\sigma_0 = 0.05\ \mathrm{N\ m^{-1}}$) at $U = 1.36\ \mathrm{m\ s^{-1}}$ and $H/R = 0.2$. The last row of images presents a zoom on the finger-like structures in order to illustrate the adaptive mesh refinement for the last timestep $t = 0.16$ s. The maximum level of mesh refinement N is equal to 9.

meniscus curvature and (ii) in the model, the effect of inertia and the backflow are not included.

In order to provide more quantitative data for the rib spacing, the air/liquid interface positions are directly extracted from the VOF data at a fixed height from the bottom ($y = 67$ cm) for various simulation times t. Figure 13 displays such spatio-temporal series of the VOF (blue: air and dark red: liquid), and the interface location (black continuous line). In all cases, the interface is initially flat and then evolves into an array of fingers at later times. These images from computations show a strong resemblance to the initial stage of digitisation, or fingering patterns, when an initially flat interface between two immiscible viscous fluids in thin gaps is displaced by the least viscous fluid among the two. They also strikingly resemble the ribbing patterns in film-splitting flows (Rabaud 1994, see figure 9). The last row of images in figure 13 presents a zoom on the finger-like structures for the last timestep $t = 0.16$ in order to illustrate the adaptive mesh refinement for the maximum level of mesh refinement N equal to 9. The level of refinement is sufficient to capture the finest structures, whether in terms of amplitude or wavelength. Similar to experimental measurements, the distance between ribs can be computed over the entire simulation time and the most probable rib spacing λ is then deduced. Figure 14(a) presents the comparison between such measured rib spacing λ from computations and the ST rib spacing λ_* (dotted line), as given by expression (3.14), when the capillary number is $Ca \gtrsim 1$ (★). The experimental rib spacing for the water/UCON mixture at $U = 1.36$ m $\mathrm{s^{-1}}$ and $H/R = 0.2$ is also given here (◯). The error bars indicate the first and the last

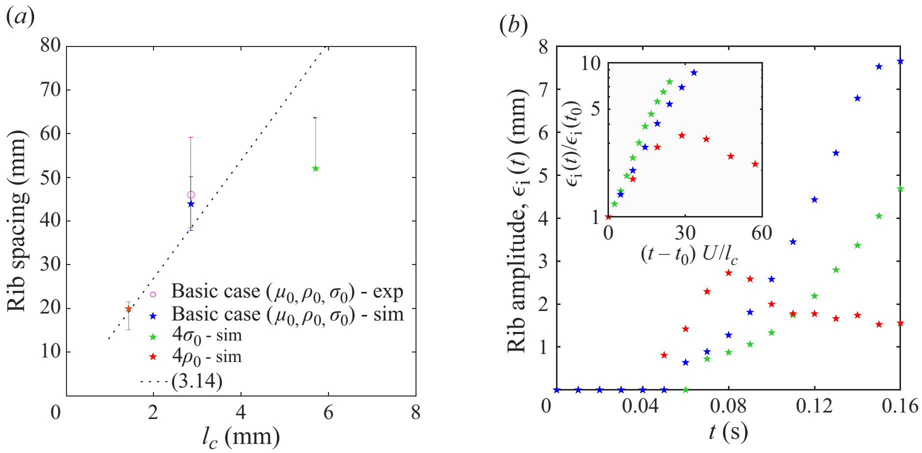

Figure 14. (a) Comparison of rib spacing between experiment (○), simulations (★) and the model (dotted line) i.e. λ_* from (3.14). The experimental data correspond to those in figure 7(g): $U = 1.36\ \mathrm{m\ s^{-1}}$ and $H/R = 0.2$ with $\rho_0 = 1044\ \mathrm{kg\ m^{-3}}$, $\mu_0 = 100$ Pa s and $\sigma_0 = 0.05\ \mathrm{N\ m^{-1}}$. ($b$) Growth of interface corrugations as a function of time for the three cases considered in numerical simulations.

quartiles of the rib spacing distribution. For the basic case, in addition to the maximum refinement level $N = 9$, the level $N = 10$ was also simulated. The value obtained for λ with $N = 10$ is within the error bar of that obtained with $N = 9$.

Firstly, the most probable rib spacing λ from both the numerical simulation (basic case) and the experimental data match very well. So, the comparison between the model (λ_*) and measured spacing λ for the basic case is also favourable, similar to what was already inferred for the experimental case, as seen for example in figure 7(c). Secondly, in the other two cases considered in the numerical simulations, a good match with the model is seen for the case $\rho = 4\rho_0$, while the rib spacing is overestimated by the model when $\sigma = 4\sigma_0$. Finally, from the spatio-temporal VOF data in figure 13, it is also possible to recover the growth of corrugation amplitude on the air/liquid interface. Let $z_i(x, t)$ be the interface location at a given time. Then, $\tilde{z}_i(x, t) = z_i(x, t) - (1/L_b)\int_0^{L_b} z_i(x, t)\mathrm{d}x$ will represent the axial variation of the perturbation about a flat interface. Thereby, for each time, we define the perturbation amplitude $\epsilon_i(t)$ as the average along the z-axis of the root-mean-square such that $\epsilon_i(t) = \sqrt{(1/L_b)\int_0^{L_b} \tilde{z}_i^2(x, t)\mathrm{d}x}$. The temporal evolution of such a perturbation amplitude is displayed in figure 14(b). For all cases, $\epsilon_i(t)$ is initially zero for a while, say up to some time t_0, and then grows very rapidly. Whereas the amplitude grows much faster for $\rho = 4\rho_0$ when compared with the basic case, it develops much slower for $\sigma = 4\sigma_0$. In addition, the interface corrugations $\epsilon_i(t)$ corresponding to the denser liquid case are observed to saturate. Indeed, as observed in figure 13(c), more and more tiny satellite droplets occur as the simulation advances from $t > 0.1$ s. This arises from insufficient spatial resolution in our simulations when $\rho = 4\rho_0$. We present in the inset of figure 14(b), data points from all cases when the renormalised amplitude $\epsilon_i(t)/\epsilon(t_0)$ are plotted on a logarithmic scale against the non-dimensional time $\tau = U(t - t_0)/l_c$. The moderate data collapse on a linear trend implies that the renormalised amplitude increases exponentially in time and l_c/U is the proper time scale for the development of ribbing patterns as in the case of the classical ST instability. These observations further confirm the relevance of the proposed phenomenology for the ribbing pattern formation.

5. Conclusions

Using a wheel of radius $R = 19.5$ cm and 30 cm width, we described axial flow patterns that appear along the wheel axis when it is rotated to drag-out liquid from a reservoir. Experiments were undertaken for two different liquid dynamic viscosities, namely, water and an approximately 100 times more viscous water/UCON mixture. When the linear speed U of the drum is increased systematically, the entrained coating flow over the drum presents rib-like patterns that consist of several liquid sheets stemming out of the bath on the rising side of the wheel. The same phenomenon occurs for various immersion depths of the wheel H/R. In all cases studied here, ribs emerge from the meniscus region in the neighbourhood where the liquid bath meets the wheel when the latter was at rest. Also, ribs often drift outward from the middle of wheel to the end walls. In general, we observed that the number of ribs approaches a normal distribution while the distribution of distance between the sheets is skewed and presents a maximum at some characteristic length that we refer to as the mostprobable rib spacing λ. Experimental measurements suggest that λ does not vary much with the drag-out speed U nor with the wheel immersion H/R considered here.

We also performed DNS using the open-source software Basilisk (Popinet 2009, 2024), which solves the incompressible two-phase Navier–Stokes equations with an explicit interface capturing method (VOF method) for three case studies. Computational domain is a cube of size 80 cm, and a solid-body rotation of angular velocity $\varOmega = 65$ rpm is applied on a half-cylinder of liquid to impose rotary dragout. Simulations with the same liquid physical parameters as the viscous water/UCON mixture on a 80 cm long wheel, namely, the basic case, were first considered. The mostprobable inter-rib distance obtained from computations showed excellent match with the experimental data. In the case where the only liquid density ρ is modified to 4 times the value in the basic case, the number of ribs is approximately doubled. In contrast, when only the liquid surface tension σ is quadrupled in the simulations, the number of ribs decreased by a factor onehalf.

We considered a mechanism analogous to the directional ST instability (Saffman & Taylor 1958; Hakim *et al.* 1990; Reinelt 1995) as the origin of such axial patterns. In the classical ST instability, when some fluid drives out a more viscous fluid in thin gaps, the interface between both fluids exhibits finger-like protuberances that grow as the interface advances. In the present liquid drag-out problem, the average air/liquid meniscus is not displaced, but remains static. However, a fluid parcel in the neighbourhood between the film and meniscus region experiences an adverse pressure gradient since the liquid flow must accommodate local wall shear and mass conservation as it rises from the liquid bath towards the film region. Thereby, the meniscus region in the drag-out flow is prone to an instability analogous to the ST instability. We modelled the rib spacing via the critical ST wavelength $\lambda_*^2 = 12\pi\sigma/|G_*|$ wherein the driving pressure gradient $|G_*|$ was taken as the average adverse pressure gradient in the meniscus region of an equivalent inclined LLD problem. Therefore, we proposed that the most probable rib spacing be estimated as $\lambda_* = 2\pi l_c\sqrt{3/\xi}$, where $\xi(Ca,\, H/R)$ is the non-dimensional average adverse pressure gradient for the corresponding inclined flat-plate drag-out flow under the lubrication approximation, and $l_c = \sqrt{\sigma/(\rho\tilde{g})}$ is the capillary length based on the effective gravity $\tilde{g}$, as computed from the plate inclination depending on the wheel immersion ratio (H/R).

We demonstrated that the proposed rib spacing λ_* is generally of the order of $15l_c$, and it matches reasonably well with measurements in all our experiments, despite the inertial and complex two-phase nature of the problem, where droplets and bubbles are formed between the liquid sheets. Numerical simulations further confirmed the proposed scaling for the spacing and for the growth rate of rib formation at different liquid physical properties, i.e. the above-mentioned doubling and the halving of the most probable rib distance was well-captured by the capillary length scaling in λ_*. In summary, our analysis based on computations and experiments strongly confirms the ribbing pattern formation in rotary drum liquid entrainment is due to a mechanism analogous to the directional ST instability (Hakim *et al.* 1990; Rabaud 1994; Reinelt 1995). Our results also suggest that the most probable inter-rib distance can be predicted from an estimate of the adverse pressure gradient via a lubrication model of an inclined drag-out flow. At this stage, it is needs to be further clarified why results from lubrication model can be relevant in such an inertial rotary LLD flow. More work is necessary to highlight the role of the wheel radius, or more generally of external wall curvature, on the axial pattern formation during inertial liquid dragout. Also, a full linear stability analysis for both the inclined-plate LLD flow and the rotary drag-out problem, similar to that of Hosoi & Mahadevan (1999), is needed to further validate and improve the proposed ST mechanism for ribbing patterns.

Supplementary materials. Supplementary materials are available at https://doi.org/10.1017/jfm.2025.51.

Acknowledgements. Authors thank A. Buridon, G. Geniquet and S. Martinez from Université Claude-Bernard Lyon 1 for their technical support in maintaining the experimental set-up and instrumentation. We also acknowledge intern students, namely, R. Cates (funded by LABEX iMUST), É. Duffaux and S. Gonin for their assistance with preliminary experiments and image processing drills.

Funding. This work was partially supported by the LABEX iMUST of the University of Lyon (ANR-10-LABX-0064), created within the ‘Plan France 2030’ set up by the french government and managed by the French National Research Agency (ANR). The numerical part of this work was granted access to the HPC resources of PMCS2I (Pôle de Modélisation et de Calcul en Sciences de l’Ingénieur et de l’Information) of École Centrale de Lyon, and P2CHPD (Pôle de Compétence en Calcul Haute Performance Dédié) of Université Lyon 1.

Declaration of interests. The authors report no conflict of interest.

REFERENCES

ADACHI, K., TAMURA, T. & NAKAMURA, R. 1988 Coating flows in a nip region and various critical phenomena. *AIChE J.* **34** (3), 456–464.

BABCHIN, A., FRENKEL, A., LEVICH, B. & SIVASHINSKY, G. 1983 Nonlinear saturation of Rayleigh–Taylor instability in thin films. *Phys. Fluids* **26** (11), 3159–3161.

BALESTRA, G., KOFMAN, N., BRUN, P.-T., SCHEID, B. & GALLAIRE, F. 2018 Three-dimensional Rayleigh–Taylor instability under a unidirectional curved substrate. *J. Fluid Mech.* **837**, 19–47.

BALMER, R.T. 1970 The hygrocyst–a stability phenomenon in continuum mechanics. *Nature* **227** (5258), 600–601.

CERRO, R. & SCRIVEN, L. 1980 Rapid free surface film flows. an integral approach. *Ind. Engng Chem. Fundam.* **19** (1), 40–50.

CHOMAZ, J.-M. 2005 Global instabilities in spatially developing flows: non-normality and nonlinearity. *Annu. Rev. Fluid Mech.* **37** (1), 357–392.

CHUOKE, R., VAN MEURS, P. & VAN DER POEL, C. 1959 The instability of slow, immiscible, viscous liquid-liquid displacements in permeable media. *Trans. AIME* **216** (1), 188–194.

COUDER, Y., MICHALLAND, S., RABAUD, M. & THOMÉ, H. 1990 *The Printer’s Instability: The Dynamical Regimes of Directional Viscous Fingering*. Springer.

COYLE, D., MACOSKO, C. & SCRIVEN, L. 1990 Stability of symmetric film-splitting between counter-rotating cylinders. *J. Fluid Mech.* **216**, 437–458.

CROSS, M. & HOHENBERG, P. 1993 Pattern formation outside of equilibrium. *Rev. Mod. Phys.* **65** (3), 851–1112.

DERYAGUIN, B. 1943 Thickness of liquid layer adhering to walls of vessels on their emptying and the theory of photo-and motion-picture film coating. In *Comptes Rendus (Doklady) De l’Academie Des Sciences De l’URSS*, vol. **39**, pp. 13–16.

DERYAGUIN, B. & LEVI, S. 1964 *Film Coating Theory*. Focal Press.

FAUVE, S. 1998 Pattern forming instabilities. In *Collection Alea-Saclay: Monographs and Texts in Statistical Physics* (ed. C. Godrèche & P. Manneville), chap. 5, pp. 387–492. Cambridge University Press.

FERMIGIER, M., LIMAT, L., WESFREID, J., BOUDINET, P. & QUILLIET, C. 1992 Two-dimensional patterns in Rayleigh–Taylor instability of a thin layer. *J. Fluid Mech.* **236**, 349–383.

GALLAIRE, F. & BRUN, P.-T. 2017 Fluid dynamic instabilities: theory and application to pattern forming in complex media. *Phil. Trans. R. Soc. Lond. A: Math. Phys. Engng Sci.* **375** (2093), 20160155.

GIORGIUTTI, F., BLETON, A., LIMAT, L. & WESFREID, J. 1995 Dynamics of a one-dimensional array of liquid columns. *Phys. Rev. Lett.* **74** (4), 538–541.

HAKIM, V., RABAUD, M., THOMÉ, H. & COUDER, Y. 1990 *Directional Growth in Viscous Fingering*. Springer.

HOMSY, G.M. 1987 Viscous fingering in porous media. *Annu. Rev. Fluid Mech.* **19** (1), 271–311.

HOSOI, A. & MAHADEVAN, L. 1999 Axial instability of a free-surface front in a partially filled horizontal rotating cylinder. *Phys. Fluids* **11** (1), 97–106.

JEFFREYS, H. 1930 The draining of a vertical plate. *Math. Proc. Camb. Phil. Soc.* **26** (2), 204–205.

JIN, B., ACRIVOS, A. & MÜNCH, A. 2005 The drag-out problem in film coating. *Phys. Fluids* **17** (10), 103603.

JOHN SOUNDAR JEROME, J., THEVENIN, S., BOURGOIN, M. & MATAS, J.-P. 2021 Inertial drag-out problem: sheets and films on a rotating disc. *J. Fluid Mech.* **908**, A7.

KHESHGI, H., KISTLER, S. & SCRIVEN, L. 1992 Rising and falling film flows: viewed from a first-order approximation. *Chem. Engng Sci.* **47** (3), 683–694.

LANDAU, L. & LEVICH, B. 1942 Dragging of a liquid by a moving plate. *Acta Physicochim. USSR* **17**, 42.

LEDDA, P.G., LERISSON, G., BALESTRA, G. & GALLAIRE, F. 2020 Instability of a thin viscous film flowing under an inclined substrate: the emergence and stability of rivulets. *J. Fluid Mech.* **904**, A23.

LERISSON, G., LEDDA, P.G., BALESTRA, G. & GALLAIRE, F. 2020 Instability of a thin viscous film flowing under an inclined substrate: steady patterns. *J. Fluid Mech.* **898**, A6.

LIMAT, L., GIORGIUTTI, F., FERMIGIER, M., JENFFER, P. & WESFREID, J.-E. 1997 Dynamique non-linéaire d'instabilités de surface: gouttes et colonnes liquides formées par ruissellement de films. *Revue générale De Thermique* **36** (9), 672–681.

MICHALLAND, S., RABAUD, M. & COUDER, Y. 1996 Instabilities of the upstream meniscus in directional viscous fingering. *J. Fluid Mech.* **312**, 125–148.

MIKAELIAN, K.O. 1996 Rayleigh–Taylor instability in finite-thickness fluids with viscosity and surface tension. *Phys. Rev. E* **54** (4), 3676–3680.

MILL, C. & SOUTH, G. 1967 Formation of ribs on rotating rollers. *J. Fluid Mech.* **28** (3), 523–529.

MOFFATT, H. 1977 Behaviour of a viscous film on the outer surface of a rotating cylinder. *Journal De Mécanique* **16** (5), 651–673.

MOSTERT, W., POPINET, S. & DEIKE, L. 2022 High-resolution direct simulation of deep water breaking waves: transition to turbulence, bubbles and droplets production. *J. Fluid Mech.* **942**, A27.

PITTS, E. & GREILLER, J. 1961 The flow of thin liquid films between rollers. *J. Fluid Mech.* **11** (1), 33–50.

POPINET, S. 2009 An accurate adaptive solver for surface-tension-driven interfacial flows. *J. Comput. Phys.* **228** (16), 5838–5866.

POPINET, S. 2024 Basilisk. http://basilisk.fr/ (open source software).

PRITCHARD, W. 1986 Instability and chaotic behaviour in a free-surface flow. *J. Fluid Mech.* **165** (1), 1–60.

RABAUD, M. 1994 Dynamiques interfaciales dans l'instabilité de l'imprimeur. *Annales De Physique France* **19** (6), 659–690.

REINELT, D. 1995 The primary and inverse instabilities of directional viscous fingering. *J. Fluid Mech.* **285**, 303–327.

SAFFMAN, P. & TAYLOR, G. 1958 The penetration of a fluid into a porous medium or hele-shaw cell containing a more viscous liquid. *Proc. R. Soc. Lond. A. Math. Phys. Sci.* **245**, 312–329.

SAVAGE, M. 1977 Cavitation in lubrication. part 1. on boundary conditions and cavity–fluid interfaces. *J. Fluid Mech.* **80** (4), 743–755.

SCHWEIZER, P. & KISTLER, S. 2012 *Liquid Film Coating: Scientific Principles and Their Technological Implications*. Springer Science & Business Media.

TAYLOR, G.I. 1923 Stability of a viscous liquid contained between two rotating cylinders. *Phil. Trans. R. Soc. Lond. A* **223** (605–615), 289–343.

THEOFILIS, V. 2011 Global linear instability. *Annu. Rev. Fluid Mech.* **43** (1), 319–352.

THORODDSEN, S. & MAHADEVAN, L. 1997 Experimental study of coating flows in a partially-filled horizontally rotating cylinder. *Exp. Fluids* **23** (1), 1–13.

VRIJ, A. 1966 Possible mechanism for the spontaneous rupture of thin, free liquid films. *Discuss. Faraday Soc.* **42**, 23–33.

WEINSTEIN, S. & RUSCHAK, K. 2001 Dip coating on a planar non-vertical substrate in the limit of negligible surface tension. *Chem. Engng Sci.* **56** (16), 4957–4969.

WEINSTEIN, S. & RUSCHAK, K. 2004 Coating flows. *Annu. Rev. Fluid Mech.* **36** (1), 29–53.

WILSON, S.D. 1982 The drag-out problem in film coating theory. *J. Engng Math.* **16** (3), 209–221.

YIH, C.-S. 1960 Instability of a rotating liquid film with a free surface. *Proc. R. Soc. Lond. A. Math. Phys. Sci.* **258**, 63–89.

ZHANG, B., POPINET, S. & LING, Y. 2020 Modeling and detailed numerical simulation of the primary breakup of a gasoline surrogate jet under non-evaporative operating conditions. *Intl J. Multiphase Flow* **130**, 103362.